Rapid decay of storm-time ring current due to pitch angle scattering in curved field line

Y. Ebihara[1*], M. –C. Fok[2], T. J. Immel[3], and P. C. Brandt[4]

1. Institute for Advanced Research, Nagoya University, Aichi, 464-8601, Japan.

2. NASA GSFC, Code 673, Greenbelt, MD 20771, USA

3. University of California, Space Science Laboratory, CA 94720-7450, USA

4. Johns Hopkins University, Applied Physics Laboratory, Laurel, MD 20723

* Now at Research Institute for Sustainable Humanosphere, Kyoto University, Uji, Kyoto 611-0011, Japan

Abstract

The storm-time ring current sometimes exhibits rapid decay, as suggested from the Dst index, but the underlying mechanism is unknown. By means of a simulation with pitch angle scattering due to the field line curvature (FLC), together with the charge exchange and adiabatic loss cone loss, we investigated rapid decay of the storm-time ring current for the large magnetic storm that occurred on 12 August 2000. When all three loss processes were included, the Dst (Sym-H) index showed rapid recovery with an *e*-folding time of ~6 h. However, without FLC scattering, the simulated Dst (Sym-H) index showed a slower recovery with an *e*-folding time of ~12 h. Overall flux of energetic neutral hydrogen with energy ≥39 keV was significantly reduced by the FLC scattering, and is consistent with data from the high energy neutral analyzer (HENA) onboard the IMAGE satellite. Power of precipitating protons showed a fairly good agreement with data from the far ultraviolet (FUV) imager onboard IMAGE. These fairly good agreements with observations lead to the possible conclusion that the FLC scattering is a significant loss mechanism for the ring current ions, and the main oval of the proton aurora is likely a manifestation of the precipitating loss of the protons for this particular storm.

1. Introduction

The terrestrial ring current consists of ions with energies ranging from a few keV to several hundred keV [e.g., Smith and Hoffman, 1973; Williams, 1981]. The growth of the ring current is primarily caused by an enhancement of the convection electric field [e.g., Wolf et al., 1982]. The ring current can be further developed by the presence of a dense plasma sheet [e.g., Chen et al., 1994; Thomsen et al., 1998; Ebihara et al., 1998; Liemohn et al, 2001] and a substorm injection [e.g., Fok et al., 1999]. Decay of the ring current occurs when (1) the ions are neutralized, (2) the ions precipitate into the ionosphere, (3) the ions are deenergized, and (4) the ion population drifts out through the dayside magnetopause while being replaced by a less dense plasma sheet source population.

Item (1) refers to *the charge exchange* reaction with neutrals [e.g., Dessler and Parker, 1959; Tinsley, 1976; Roelof, 1985]. Hamilton et al. [1988] found that the energy density of O^+ dominated that of H^+ near the Dst minimum during the February 1986 storm, and suggested that a rapid recovery of Dst (~9.3 h) results largely from the rapid loss of O^+ with an energy of 75–100 keV via charge exchange at L = 2–3. Fok et al. [1995] simulated the ring current for the February 1986 storm, and concluded that the charge exchange cannot account for the rapid Dst recovery. Kozyra et al. [1998] suggested that in addition to the charge exchange, the precipitation loss into the ionosphere plays a major role in the rapid Dst recovery. Keika et al. [2006] used observation of energetic neutral atoms emitted from the ring current, and concluded that the charge exchange cannot fully explain the

rapid decay of the ring current.

Item (2) refers to the precipitation loss. During magnetic storms, a filled loss cone with completely/almost isotropic pitch angle distribution has been observed in the auroral/subauroral region at low altitudes [e.g., Amundsen et al., 1972; Hultqvist et al., 1976; Sergeev et al., 1983; 1993; Søraas et al., 1999], at mid altitudes [e.g., Walt and Voss, 2001], and at high altitudes [e.g., Williams and Lyons, 1974]. The latitude of the boundary between the isotropic and anisotropic proton precipitation (which is called the isotropic boundary) moves equatorward when the magnetic field is stretched [Sergeev et al., 1993]. The isotropic boundary is collocated well with the maximum of energy flux of ion precipitation [Newell et al., 1998].

The following four distinct mechanisms have been suggested to explain the enhanced precipitation of ions: (2a) *The adiabatic loss cone loss* occurs when ions drift earthward and their equatorial pitch angle shifts toward 90° due to the conservation of the first two adiabatic invariants. The loss cone angle is also rapidly widened as the ions drift earthward. Thus, ions with a small pitch angle encounter the loss cone at a certain L-value without any pitch angle scattering. Jordanova et al. [1996] suggested that the adiabatic loss cone loss is sufficient to explain the overall precipitation of the ions observed by satellites. However, Ebihara and Ejiri [2003] showed that the contribution from the adiabatic loss cone loss only amounts to ~1–2% of the ring current loss during weak magnetic storms. (2b) *The Coulomb scattering* with thermal plasma is likewise thought to

make only a minor contribution to the decay of ions at energies >15 keV [Jordanova et al., 1996; 1997] because the deflection angle due to the Coulomb scattering is inversely proportional to energy. (2c) Ions can be scattered by *the wave-particle interaction*, namely, the electromagnetic ion cyclotron (EMIC) waves that are frequently observed in the inner magnetosphere [e.g., Anderson et al., 1992]. Simulation efforts have been made to understand the generation of EMIC waves and their contribution to the ring current [e.g., Jordanova et al., 1997; 2006; Khazanov et al., 2007; Gamayunov and Khazanov, 2008]. Jordanova et al. [1997; 2006] suggested that EMIC waves are developed near the plasmapause or inside the plasmaspheric plumes, and reduce the total energy by ~10%. Isolated long-lasting proton precipitation and localized spots of proton auroral emissions in the subauroral region are thought to result from precipitation of the protons scattered by the EMIC waves [e.g., Gvozdevsky et al., 1997; Fuselier et al. 2004; Spasojevic et al. 2005; Jordanova et al. 2007]. (2d) Ions are scattered when they travel through a region where the gyroradius of the ion is close to the curvature radius of a field line [e.g., Sergeev et al. 1983, Birmingham, 1984; Büchner and Zelenyi 1989, Delcourt et al. 1996; Young et al., 2002; 2008]. Hereinafter, this scattering mechanism is referred to as *field line curvature (FLC) scattering*. Ion precipitation with an isotropic pitch angle distribution is suggested to result from the FLC scattering [e.g., Sergeev et al., 1993] based on low-altitude particle observations and high-altitude magnetic field observations. The overall contribution of the FLC scattering to the ring current decay is not yet understood.

Item (3) refers to *Coulomb drag*. The energy of ions can be degraded by Coulomb drag

when the ions move through a thermal plasma [Spitzer, 1962; Cole, 1965]. As a consequence, the velocity space distribution of the ions is redistributed [Fok et al., 1995; Jordanova et al., 1996]. The Coulomb drag is thought to be insignificant for ring current decay because the loss rate is much smaller than that of the charge exchange [Fok et al., 1991], and the interaction between the ring current ions and the plasmasphere occurs in a limited region.

Item (4) refers to c*onvection outflow*. The ring current can decay when the ion population that contributes to the ring current is drained toward the dayside magnetopause by the convection electric field, and is replaced by a newly injected tenuous ion population from the nightside plasma sheet [e.g., Ebihara and Ejiri, 1998; Liemohn et al., 2001 ; Keika et al., 2005]. The ring current decays when the number of outgoing particles exceeds that of incoming particles. The decay rate of the ring current is determined by the degree of imbalance between incoming particles and outgoing particles. Multipoint observations of incoming particles on the nightside and outgoing particles on the dayside are necessary to evaluate the net loss of the ion population in the ring current due to the convection outflow.

The purpose of this study is to investigate the decay of the ring current due to the FLC scattering, whose overall contribution to the ring current decay is unknown. We performed a simulation of the ring current, including the FLC scattering, charge exchange, and adiabatic loss cone loss. The results were compared with the Dst*(Sym-H*) index, and global distributions of energetic neutral hydrogen and the Doppler-shifted Lyman α

emission (proton aurora).

2. Simulation

We used the comprehensive ring current model (CRCM) [Fok et al., 2001] to solve the evolution of the four-dimensional phase-space density of hot protons in the inner magnetosphere. The phase space density *f* is a function of the magnetic latitude (MLAT), magnetic local time (MLT), first adiabatic invariant, and second adiabatic invariant. The evolution of *f* is written as

$$\begin{aligned}
&\frac{\partial f}{\partial t}+\left\langle \dot{\lambda}_i \right\rangle \frac{\partial f}{\partial \lambda_i}+\left\langle \dot{\varphi}_i \right\rangle \frac{\partial f}{\partial \varphi_i} \\
&=-\left(\frac{f}{0.5\tau_b}\right)_{\text{LOSS CONE}} \\
&\quad -v\sigma_s \left\langle n_H \right\rangle f \\
&\quad +\frac{1}{T(\alpha_0)\sin 2\alpha_0}\frac{\partial}{\partial \alpha_0}\left(T(\alpha_0)\sin 2\alpha_0 D_{\alpha_0\alpha_0}\frac{\partial f}{\partial \alpha_0}\right),
\end{aligned} \tag{1}$$

where $\lambda_i, \varphi_i, v, \sigma_s, n_H, \tau_b, \alpha_0,$ and $D_{\alpha_0\alpha_0}$ are the magnetic latitude, magnetic longitude, speed of the particle, charge exchange cross section, neutral hydrogen density, bounce period, equatorial pitch angle, and pitch angle diffusion coefficient, respectively. The first three terms on the right hand side represent the proton loss inside the loss cone, loss due to the charge exchange, and pitch angle diffusion, respectively. Readers may refer to Fok et al. [2001] for a detailed explanation of this model.

We used the diffusion coefficient that was previously formulated by Young et al. [2008] as

$$D_{\alpha_0\alpha_0} = \frac{DN^2 \sin^2\left[\omega(\varepsilon)\alpha_0\right]\cos^{2b(\varepsilon)}(\alpha_0)}{\sin^2(\alpha_0)\cos^2(\alpha_0)}, \tag{2}$$

$$D \equiv \frac{A^2(\varepsilon,\zeta_1,\zeta_2)}{2\tau_b}, \tag{3}$$

$$N \equiv \left[\sin(\omega(\varepsilon)\alpha_0)\cos^{b(\varepsilon)}(\alpha_0)\right]^{-1}\Big|_{\alpha_0=\bar{\alpha}_0}, \tag{4}$$

$$A \equiv \exp(c(\varepsilon))\left(\zeta_1^{a_1(\varepsilon)}\zeta_2^{a_2(\varepsilon)} + D(\varepsilon)\right), \tag{5}$$

where $\varepsilon = r_G/r_c$, where r_G is the gyroradius in the equatorial plane and r_c is the curvature radius of a field line in the equatorial plane. Here, $\zeta_1 = r_c(\partial^2 r_c / \partial s^2)$ and $\zeta_2 = (r_c^2 / B_0)(\partial^2 B_0 / \partial s^2)\big|_0$ are measures of the changing equatorial curvature radius r_c and the equatorial magnetic field B_0, respectively, and s is the distance along the magnetic field line. $\bar{\alpha}_0$ is the equatorial pitch angle at which the A value reaches its maximum. The parameters, $\omega(\varepsilon)$, $a_1(\varepsilon)$, $a_2(\varepsilon)$, $b(\varepsilon)$, $c(\varepsilon)$, and $D(\varepsilon)$, are given by quadratic polynomial forms [Young et al., 2002; 2008]. When ε>0.584, we set ε=0.584 [Young et al., 2008]. When ε<0.1, we don't calculate the pitch angle diffusion because the diffusion coefficient is too small.

The FLC scattering takes place twice each bounce period in the equatorial plane, so that the diffusion coefficient is not necessary to be bounce-averaged. The TS04 magnetic field model [Tsyganenko et al., 2003; Tsyganenko and Sitnov, 2005] was employed to represent the storm-time magnetic field in the inner magnetosphere. The Weimer 2005 electric field

model [Weimer, 2005] was used to impose the electric potential to the poleward boundary at the ionospheric altitude. The Weimer 2005 model reproduces nonlinear saturation effects in the solar wind-magnetosphere coupling. The input parameters for the TS04 model and the Weimer 2005 model were determined using the 5-min resolution of the OMNI2 data set [King and Papitashvili, 2005].

We focused on the magnetic storm that occurred on 12 August 2000 because the apogee of the IMAGE satellite was situated above the North Pole during the most developed period of the storm. The solar wind, interplanetary magnetic field (IMF), and Sym-H* index are summarized in Figure 1. The time of the solar wind and IMF data were shifted from the observation position of the satellite to the bow shock nose of the Earth [King and Papitashvili, 2005]. The Dst* (Sym-H*) index was obtained based on the observed Dst (Sym-H) index with a correction for the solar wind dynamic pressure [Gonzalez et al., 1994]. It should be noted that the Dst* (Sym-H*) index is the appropriate index, and may still include contributions from the magnetopause current, the field-aligned current, and the ionospheric current.

No geosynchronous satellites measured hot ions on the nightside during the main phase of this storm. We used the differential proton intensity measured by Polar/MICS [Wilken et al., 1992; Roeder, 2005] at L = 6.6 and 0253 MLT near the equatorial plane at 0922 UT on 12 August 2000. The differential flux was fitted to the double-Maxwellian distribution. The fitted parameters are as follows: a density of 0.23 cm^{-3} and temperature of 2.7 keV for

the first Maxwellian, and a density of 0.13 cm^{-3} and temperature of 26 keV for the second Maxwellian. The double-Maxwellian distribution was imposed to the outer boundary of the simulation.

In order to isolate the influence of the loss processes, three different simulations were performed: Run 1 included (1) the charge exchange loss, (2a) the adiabatic loss cone loss, and (2d) the FLC scattering. Run 2 included (1) the charge exchange loss and (2a) the loss cone loss. Run 3 included only (2a) the loss cone loss. All of the other parameters had the same settings. These simulation settings are summarized in Table 1.

3. Results

Figure 2 shows the calculated plasma pressure perpendicular to the magnetic field at 0840 UT on 12 August 2000 (in the late main phase). The plasma pressure was well developed at around L = 2–3 on the nightside. When the FLC scattering was included (Run 1), the plasma pressure was significantly decreased in the outer ring current in comparison with that in Runs 2 and 3.

Figure 3 shows ratio between the curvature radius of a field line and the gyroradius of 50 keV protons in the equatorial plane (i.e., the ε value in (2)) for 0840 UT on 12 August 2000. The ratio is greater than 0.1 on the nightside at $L \geq 5$ due to the stretched and weak

magnetic field.

In Figure 4, we show the pitch angle distributions (PADs) of the protons at 50 keV at midnight at L = 4 (left) and L = 5 (right). At L = 4, the ε value is ~0.029 at midnight, so that the pitch angle diffusion is not calculated. The loss cone is almost empty for Runs 1 and 2 (left). At L = 5, the ε value is ~0.12 at midnight and the diffusion coefficient is relatively large (~4×10^{-4} s^{-1} at the equatorial pitch angle of 10° at midnight) for Run 1. The protons are effectively scattered, and the loss cone is completely filled by the FLC scattering for Run 1. The maximum of $D_{\alpha_0\alpha_0}\tau_b$ is 0.13 at this moment, so that the FLC scattering is small on the bounce period time scale. The nearly isotropic PAD around the loss cone are consistent with the in-situ satellite observations [e.g., Amundsen et al., 1972; Hultqvist et al., 1976; Sergeev et al., 1983; 1993; Søraas et al., 1999].

The left panel of Figure 5 shows the energy flux of precipitating protons obtained by the Doppler-shifted Lyman α images captured by a far ultraviolet (FUV) imager on board the IMAGE satellite [Mende et al., 2002a; 2002b]. See Hubert et al. [2002] and Frey et al. [2003] for the derivation of the energy flux of precipitating protons from the auroral images. The equatorward boundary of the observed proton precipitation was located at ~55 MLAT at midnight at 0840 UT on 12 August 2000. Coumans et al. [2002] compared the IMAGE/FUV observation with particle data obtained from the NOAA-TIROS satellite at 1011–1020 UT on 12 August 2000. They demonstrated that the energy flux based on the IMAGE/FUV observation shows a satisfactory agreement with the in-situ particle

observations.

The middle panel of Figure 5 shows the simulated energy flux of precipitating protons for Run 1. The precipitation occurs in the oval-shaped region with its peak flux taking place near midnight. When only the adiabatic loss cone loss is included (Run 2), the energy flux is lower compared to that of Run 1 and the precipitation occurs in a latitudinally confined region, which is inconsistent with the observations.

Power of precipitating protons into the ionosphere (Ψ) can be derived by the following equation:

$$\Psi = 2 \times \iint F(\lambda, \phi) r^2 \cos(\lambda) d\lambda d\phi, \quad (6)$$

where F and r are the precipitating energy flux and the geocentric distance of the ionosphere altitude (100 km altitude), respectively, assuming that the same quantity of protons was precipitating into both hemispheres. Since the Doppler-shifted Lyman α images were slightly contaminated by the solar radiance on the dayside, the integration was performed only on the nightside, that is, from 1800 MLT to 0600 MLT.

Figure 6 shows the power of precipitating protons. The observed power (solid line) reached its maximum value of ~3×10^{26} keV s^{-1} at ~0910 UT, and gradually decayed in the early recovery phase. The power is consistent with that derived by Fang et al. [2007] who used data from the polar orbiting satellite, NOAA. In Run 1, the power was ~1.5×10^{26} keV s^{-1} at ~0630 UT, and decayed gradually over time, which is consistent with the

observation. In Run 2, the maximum power was ~4 × 10^{25} keV s^{-1}, which is an order of magnitude smaller than the observation, indicating that the adiabatic loss cone loss cannot account for the observation of proton precipitation. The FLC scattering might sufficiently explain the power of the nightside proton precipitation within a factor of ~2.

Figure 7 compares the observed Sym-H* index with the calculated ones. At 1025 UT, the observed Sym-H* started to show a rapid recovery, followed by a slow recovery. An *e*-folding decay time of the observed Sym-H* during the initial rapid recovery was ~3 h. In Run 1 (red line), the Sym-H* index also showed an initial rapid recovery (starting at ~0900 UT) with an *e*-folding decay time of ~6 h. The *e*-folding decay time was ~12 h in Run 2 (blue line), and ~28 h in Run 3 (green line).

Figures 8a summarizes composite images of the number flux of energetic hydrogen (reddish color) at 39–50 keV together with the energy flux of precipitating protons (bluish color) from the vantage point of the IMAGE satellite. The energetic hydrogen was emitted from the region where a proton undergoes a charge exchange process in a collision with exospheric neutral hydrogen or neutral oxygen of the upper atmosphere, and was observed by a high energy neutral analyzer (HENA) on board the IMAGE satellite [Mitchell et al., 2000]. The energy flux of the precipitating protons is the same as Figure 5, and was obtained based on the Doppler-shifted Lyman α emission remotely captured by IMAGE/FUV [Mende et al., 2000a; 2000b]. Thus, the composite image is a direct representation of the two major loss processes of the ring current, that is, the charge

exchange (reddish color) and precipitation into the ionosphere (bluish color). The peak intensity of the observed energetic hydrogen occurred in the post-midnight, which was previously reported [Brandt et al., 2002]. The post-midnight enhancement of the peak intensity of the energetic hydrogen is attributed to the skewed electric potential that resulted from the ring current [Fok et al., 2003; Ebihara and Fok, 2004].

Figures 8b and 8c are the same as Figure 8a, but were obtained by the simulation. The number flux of the energetic hydrogen was calculated by the line of sight integral as

$$j_{EH} = \sigma_s \int n_H j_P dl, \tag{7}$$

where j_p is the differential flux of the protons, and dl is a line element along the line of sight from the IMAGE satellite [Roelof, 1987; Fok et al., 2003]. The maximum intensity of the energetic hydrogen is larger than that of the observed one, but overall morphology of the simulated distribution of the energetic hydrogen is consistent with the observation.

Figure 9 shows time history of the integrated energetic hydrogen flux. The integration was performed by using the images of the neutral hydrogen shown in Figure 8 over 45° from the center of the Earth with the following equation

$$J_{EH} = \int_{E_1}^{E_2} \int j_{EH} dE d\Omega, \tag{8}$$

where E is the kinetic energy, and Ω is the solid angle. The integrated flux shows a gradual decrease in the first half of the period in the outbound pass, and a gradual increase in the second half of the period in the inbound pass of its orbit. This gradual change in the

flux is primarily due to a geometrical effect [e.g., Ohtani et al., 2006]. The most intense emission of energetic hydrogen is confined to a region near the Earth as shown in Figure 9 (i.e., the source can be approximated as a point source), so that the integrated flux tends to decrease with the geocentric distance. In addition, the pitch angle distribution of seed protons is known to influence the global distribution of energetic hydrogen [e.g., Perez et al., 2001; Ohtani et al., 2005]. The dotted and dashed lines stand for the simulated flux in Run 1 and Run 2, respectively. At energy 10–39 keV (Figure 9a), both the simulated fluxes are almost the same with each other because the gyroradius of the 10–39 keV protons are too small to occur the FLC scattering significantly. In general, the simulated flux is larger than observed. The difference between the simulation and the observation is attributed to the assumed pitch angle distribution and the energy distribution of protons at the simulation boundary, but is beyond the scope of this study. At energy 39–119 keV (Figure 9b), the simulated flux in Run 1 is smaller than in Run 2 by a factor of ~2, and is closed to the one observed when IMAGE was located at radial distance ≥6 Re (~0900–1700 UT). The significant reduction of the energetic hydrogen in Run 1 implies that the FLC scattering is effective for reducing the overall protons with energy ≥39 keV.

4. Discussion

In Run 1, the ring current decayed rapidly with an *e*-folding time of ~6 h at the beginning of the recovery phase. This *e*-folding time is consistent with typical decay time values of

5–10 h during magnetic storms [Gonzalez et al., 1994 and references therein]. Kozyra et al. [1998] compiled the precipitating ion fluxes observed by the low-altitude satellites NOAA and DMSP, and derived the lifetime of the order of 8–10 h or less for the precipitating loss during the February 1986 storm. The global morphology and intensity of the proton precipitation were fairly consistent with the IMAGE/FUV observations within a factor of 2. The results of Run 1 suggest that the FLC scattering may sufficiently explain the decay of the storm-time ring current, and the global precipitation of protons.

Unfortunately, we cannot easily make a direct comparison with the observed Sym-H* (Dst*) index because Sym-H* (Dst*) includes contributions not only from the ring current, but also from the tail current, field-aligned current, and ionospheric current. Ohtani et al. [2005] suggested that the rapid recovery of Sym-H* starting at 1024 UT on 12 August 2000 was caused by a sudden collapse of the tail current associated with a substorm. Run 1 showed that the rapid recovery of Sym-H* occurred at ~0920 UT, which is earlier than observed. The earlier onset of the rapid recovery may be explained by the uncertainty in the travel time of the solar wind condition to the inner magnetosphere, or by the exclusion of the contribution from the tail current to the simulated Sym-H*.

Of course, we cannot rule out the other processes. Jordanova et al. [2006] calculated the evolution of the ring current together with the pitch angle scattering by the electromagnetic ion cyclotron (EMIC) waves. They calculated the wave growth and pitch angle diffusion coefficient under the quasi-linear theory, and concluded that the pitch angle scattering due

to the EMIC waves reduced the total proton energy of the ring current by ~10% during the storm recovery phase. Recently, Omura et al. [2010] derived wave equations that describe the nonlinear behavior of the trapped protons interacting with the EMIC waves, called the EMIC chorus. The EMIC chorus could have resulted in the strong proton scattering and precipitation into the ionosphere.

The convection outflow of particles has been thought to contribute significantly to the ring current decay [e.g., Ebihara and Ejiri, 1998; Liemohn et al., 2001; Keika et al., 2005]. This mechanism becomes significant when the plasma sheet density (which is a source of ring current ions) drops suddenly, with a time scale shorter than that of the convection electric field. Unfortunately, no geosynchronous satellite observed the plasma sheet ions on the nightside during the recovery phase. Therefore, the influence of the convection outflow cannot be investigated. It can be said that, for this particular storm, the convection outflow seems to be unnecessary to explain the rapid decay of the ring current because the FLC scattering satisfactorily explains the rapid decay of the ring current.

We assumed that the ring current consist of protons only in the simulation. Previous studies have shown that the contribution from oxygen ions is not negligible for intense magnetic storms [e.g., Hamilton et al., 1988; Daglis et al., 1999]. Exclusion of the oxygen ions could have some impacts on the simulation results. First, when the oxygen ions are included, the intensity of the ring current would be stronger. Secondly, the oxygen ring current would decay more rapidly because the FLC scattering is more effective in the

reduction of the oxygen ions that have larger gyroradius. Thirdly, the intensity of the shielding electric field would be stronger. The strong shield electric field impedes the earthward penetration of the ions from the nightside plasma sheet, so that the intensity of the ring current does not increase much [Ebihara et al., 2005]. This effect may reduce the first concern that the simulated ring current is underestimated too much. For these reasons, it can be said that our simulation may provide lower limit of the rapid decay of the ring current.

5. Conclusion

We obtained the following conclusions.

1. The Dst (Sym-H) index showed rapid recovery with the *e*-folding time of ~6 h when the FLC scattering, charge exchange and adiabatic loss cone loss were fully included. The *e*-folding time was ~12 h when the FLC scattering is excluded. The *e*-folding time is ~28 h when the charge exchange was further excluded. The *e*-folding time of ~6 h is consistent with typical one during magnetic storms.
2. The FLC scattering is efficient for decaying the overall protons with energy ≥39 keV, and is the major loss mechanism for the ring current for the 12 August 2000 storm. The charge exchange and the adiabatic loss cone loss are insufficient to explain the overall decay of the ring current.
3. Formation of the main oval of the storm-time nightside aurora can be sufficiently

explained by the precipitating protons under the influence of the FLC scattering. The calculated power of the protons precipitating into the ionosphere is consistent with the IMAGE/FUV observation.

Acknowledgments

The Dst index was provided by WDC Kyoto. The OMNI data were obtained from the GSFC/SPDF OMNIWeb interface at http://omniweb.gsfc.nasa.gov/. The authors thank Nikolai A. Tsyganenko for the empirical magnetic field model and Daniel R. Weimer for the empirical convection electric field model. The work of YE is supported by the Program for Improvement of Research Environment for Young Researchers from the Special Coordination Funds for Promoting Science and Technology (SCF) commissioned by the Ministry of Education, Culture, Sports, Science and Technology (MEXT) of Japan. This study is also supported by a Grant-in-Aid for Scientific Research (B) (19340141) by the Japan Society for the Promotion of Science (JSPS).

References

Anderson, B. J., R. E. Erlandson, and L. J. Zanetti (1992), A statistical study of Pc 1-2 magnetic pulsations in the equatorial magnetosphere, 1. Equatorial occurrence

distributions, J. Geophys. Res., 97(A3), 3075-3088, doi:10.1029/91JA02706.

Amundsen, R., F. Søraas, H. Lindalen, and K. Aarsnes (1972), Pitch-angle distributions of 100- to 300- keV protons measured by the Esro IB satellite, J. Geophys. Res., 77(4), 556-566.

Birmingham, T. (1984), Pitch angle diffusion in the Jovian magnetodisc, J. Geophys. Res., 89(A5), 2699-2707.

Brandt, P. C., S. Ohtani, D. G. Mitchell, M. -C. Fok, E. C. Roelof, and R. Demajistre (2002), Global ENA observations of the storm mainphase ring current: Implications for skewed electric fields in the inner magnetosphere, Geophys. Res. Lett., 29(20), 1954, doi:10.1029/2002GL015160.

Büchner, J. and L. Zelenyi (1989), Regular and chaotic charged particle motion in magnetotaillike field reversals, 1. Basic theory of trapped motion, J. Geophys. Res. 94, 11,821-11,842.

Chen, M. W., L. R. Lyons, and M. Schulz (1994), Simulations of phase space distributions of storm time proton ring current, J. Geophys. Res., 99(A4), 5745-5759.

Cole, K. D. (1965), Stable Auroral Red Arcs, Sinks for Energy of D st Main Phase, J.

Geophys. Res., 70(7), 1689–1706.

Coumans, V., J.-C. Gérard, B. Hubert, and D. S. Evans, Electron and proton excitation of the FUV aurora: Simultaneous IMAGE and NOAA observations, J. Geophys. Res., 107(A11), 1347, doi:10.1029/2001JA009233, 2002.

Daglis, I. A., R. M. Thorne, W. Baumjohann, and S. Orsini (1999), The terrestrial ring current: Origin, formation, and decay, Rev. Geophys., 37(4), 407–438, doi:10.1029/1999RG900009.

Delcourt, D. C., J. -A. Sauvaud, R. Martin Jr., and T. E. Moore (1996), On the nonadiabatic precipitation of ions from the near-Earth plasma sheet, J. Geophys. Res. 101, 17,409-17,418.

Dessler, A. J., and E. N. Parker (1959), Hydrodynamic theory of geomagnetic storms, J. Geophys. Res., 64, 2239.

Ebihara, Y., and M. Ejiri (1998), Modeling of solar wind control of the ring current buildup: A case study of the magnetic storms in April 1997, Geophys. Res. Lett., 25(20), 3751-3754.

Ebihara, Y., and M. Ejiri (2003), Numerical simulation of the ring current: Review, Space

Sci. Rev., 105, 377.

Ebihara, Y. and M. -C. Fok (2004), Postmidnight storm-time enhancement of tens of keV proton flux, J. Geophys. Res., 109, A12209, doi:10.1029/2004JA010523.

Ebihara, Y., M. - C. Fok, R. A. Wolf, M. F. Thomsen, and T. E. Moore (2005), Nonlinear impact of plasma sheet density on the storm-time ring current, J. Geophys. Res., 110, A02208, doi:10.1029/2004JA010435.

Fang, X., M. W. Liemohn, J. U. Kozyra, D. S. Evans, A. D. DeJong, and B. A. Emery (2007), Global 30–240 keV proton precipitation in the 17–18 April 2002 geomagnetic storms: 1. Patterns, J. Geophys. Res., 112, A05301, doi:10.1029/2006JA011867.

Fok, M. -C., J. U. Kozyra, A. F. Nagy, and T. E. Cravens (1991), Lifetime of ring current particles due to Coulomb collisions in the plasmasphere, J. Geophys. Res., 96(A5), 7861-7867.

Fok, M. -C., J. U. Kozyra, A. F. Nagy, C. E. Rasmussen, and G. V. Khazanov (1993), Decay of equatorial ring current ions and associated aeronomical consequences, J. Geophys. Res., 98(A11), 19381-19393.

Fok, M. -C., T. E. Moore, J. U. Kozyra, G. C. Ho, and D. C. Hamilton (1995),

Three-dimensional ring current decay model, J. Geophys. Res., 100(A6), 9619-9632.

Fok, M. -C., T. E. Moore, and D. C. Delcourt (1999), Modeling of inner plasma sheet and ring current during substorms, J. Geophys. Res., 104(A7), 14557-14569.

Fok, M. -C., R. A. Wolf, R. W. Spiro, and T. E. Moore (2001), Comprehensive computational model of Earth's ring current, J. Geophys. Res., 106, 8417.

Fok, M. -C., et al. (2003), Global ENA image simulations, Space Sci. Rev., 109, 77.

Frey, H. U., T. J. Immel, S. B. Mende, J. -C. Gerard, B. Hubert, S. Habraken, J. Spann, G. R. Gladstone, D. V. Bisikalo, and V. I. Shematouth (2003), Summary of quantitative interpretation of IMAGE far ultraviolet aurorae data, Space Sci. Rev., 109, 255.

Fuselier, S. A., S. P. Gary, M. F. Thomsen, E. S. Claflin, B. Hubert, B. R. Sandel, and T. J. Immel (2004), Generation of transient dayside subauroral proton precipitation, J. Geophys. Res., 109, A12227, doi:10.1029/2004JA010393.

Gamayunov, K. V., and G. V. Khazanov (2008), Crucial role of ring current H+ in electromagnetic ion cyclotron wave dispersion relation: Results from global simulations, J. Geophys. Res., 113, A11220, doi:10.1029/2008JA013494.

Gonzalez, W. D., J. A. Joselyn, Y. Kamide, H. W. Kroehl, G. Rostoker, B. T. Tsurutani, and V. M. Vasyliunas (1994), What is a geomagnetic storm?, J. Geophys. Res., 99, 5771.

Gvozdevsky, B. B., V. A. Sergeev, and K. Mursula (1997), Long lasting energetic proton precipitation in the inner magnetosphere after substorms, J. Geophys. Res., 102(A11), 24333-24338.

Hamilton, D. C., G. Gloeckler, F. M. Ipavich, W. Stüdemann, B. Wilken, and G. Kremser (1988), Ring current development during the great geomagnetic storm of February 1986, J. Geophys. Res., 93(A12), 14343-14355.

Hubert, B., J. -C. Gerard, D. S. Evans, M. Meurant, S. B. Mende, H. U. Frey, and T. J. Immel (2002), Total electron and proton energy input during auroral substorms: Remote sensing with IMAGE-FUV, J. Geophys. Res., 107(A8), 1183, doi:10.1029/2001JA009229.

Hultqvist, B., W. Riedler, and H. Borg, Ring current protons in the upper atmosphere within the plasmasphere, Planet. Space Sci., 24, 783–797, 1976.

Jordanova, V. K., L. M. Kistler, J. U. Kozyra, G. V. Khazanov, and A. F. Nagy (1996), Collisional losses of ring current ions, J. Geophys. Res., 101(A1), 111–126.

Jordanova, V. K. , J. U. Kozyra, A. F. Nagy, and G. V. Khazanov (1997), Kinetic model of the ring current‐atmosphere interactions, J. Geophys. Res., 102(A7), 14279-14291.

Jordanova, V. K., Y. S. Miyoshi, S. Zaharia, M. F. Thomsen, G. D. Reeves, D. S. Evans, C. G. Mouikis, and J. F. Fennell (2006), Kinetic simulations of ring current evolution during the Geospace Environment Modeling challenge events, J. Geophys. Res., 111, A11S10, doi:10.1029/2006JA011644.

Jordanova, V. K., M. Spasojevic, and M. F. Thomsen (2007), Modeling the electromagnetic ion cyclotron wave-induced formation of detached subauroral proton arcs, J. Geophys. Res., 112, A08209, doi:10.1029/2006JA012215.

Keika, K., M. Nosé, S.-I. Ohtani, K. Takahashi, S. P. Christon, and R. W. McEntire (2005), Outflow of energetic ions from the magnetosphere and its contribution to the decay of the storm time ring current, J. Geophys. Res., 110, A09210, doi:10.1029/2004JA010970.

Keika, K., M. Nosé, P. C. Brandt, S. Ohtani, D. G. Mitchell, and E. C. Roelof (2006), Contribution of charge exchange loss to the storm time ring current decay: IMAGE/HENA observations, J. Geophys. Res., 111, A11S12, doi:10.1029/2006JA011789.

Khazanov, G. V., K. V. Gamayunov, D. L. Gallagher, J. U. Kozyra, and M. W. Liemohn (2007), Self-consistent model of magnetospheric ring current and propagating electromagnetic ion cyclotron waves: 2. Wave-induced ring current precipitation and thermal electron heating, J. Geophys. Res., 112, A04209, doi:10.1029/2006JA012033.

King, J. H., and N. E. Papitashvili (2005), Solar wind spatial scales in and comparisons of hourly wind and ACE plasma and magnetic field data, J. Geophys. Res., 110, A02104, doi:10.1029/2004JA010649.

Kozyra, J. U., M. -C. Fok, E. R. Sanchez, D. S. Evans, D. C. Hamilton, and A. F. Nagy (1998), The role of precipitation losses in producing the rapid early recovery phase of the Great Magnetic Storm of February 1986, J. Geophys. Res., 103(A4), 6801?6814.

Liemohn, M. W., J. U. Kozyra, M. F. Thomsen, J. L. Roeder, G. Lu, J. E. Borovsky, and T. E. Cayton (2001), Dominant role of the asymmetric ring current in producing the stormtime Dst*, J. Geophys. Res., 106(A6), 10, 883-10,904.

Mende, S. B., et al. (2002a), Far ultraviolet imaging from the IMAGE spacecraft: 2. Wideband FUV imaging, Space Sci. Rev., 91, 271.

Mende, S. B., et al. (2000b), Far ultraviolet imaging from the IMAGE spacecraft. 3. Spectral imaging of Lyman-α and OI 135. 6 nm, Space Sci. Rev., 91, 287

Mitchell, D. G., et al. (2000), High energy neutral atom (HENA) imager for the IMAGE mission, Space Sci. Rev., 91, 67.

Newell, P. T., V. A. Sergeev, G. R. Bikkuzina, and S. Wing (1998), Characterizing the state of the magnetosphere: Testing the ion precipitation maxima latitude (b2i) and the ion isotropy boundary, J. Geophys. Res., 103(A3), 4739-4745.

Ohtani, S., M. Nosé, G. Rostoker, H. Singer, A. T. Y. Lui, and M. Nakamura (2001), Storm-substorm relationship: Contribution of the tail current to Dst, J. Geophys. Res., 106(A10), 21,199-21,209.

Ohtani, S., P. C. Brandt, D. G. Mitchell, H. Singer, M. Nosé, G. D. Reeves, and S. B. Mende (2005), Storm‐substorm relationship: Variations of the hydrogen and oxygen energetic neutral atom intensities during storm‐time substorms, J. Geophys. Res., 110, A07219, doi:10.1029/2004JA010954.

Ohtani, S., P. C. Brandt, H. J. Singer, D. G. Mitchell, and E. C. Roelof (2006), Statistical characteristics of hydrogen and oxygen ENA emission from the storm-time ring current, J. Geophys. Res., 111, A06209, doi:10.1029/2005JA011201.

Omura, Y., J. Pickett, B. Grison, O. Santolik, I. Dandouras, M. Engebretson, P. M. E.

Décréau, and A. Masson (2010), Theory and observation of electromagnetic ion cyclotron triggered emissions in the magnetosphere, J. Geophys. Res., 115, A07234, doi:10.1029/2010JA015300.

Perez, J. D., G. Kozlowski, P. C:son Brandt, D. G. Mitchell, J. -M. Jahn, C. J. Pollock, and X. X. Zhang (2001), Initial ion equatorial pitch angle distributions from medium and high energy neutral atom images obtained by IMAGE, Geophys. Res. Lett., 28(6), 1155–1158.

Roeder, J. L., M. W. Chen, J. F. Fennell, and R. Friedel (2005), Empirical models of the low-energy plasma in the inner magnetosphere, Space Weather, 3, S12B06, doi: 10.1029/2005SW000161.

Roelof, E. C., D. G. Mitchell, and D. J. Williams (1985), Energetic Neutral Atoms (E ~ 50 keV) from the ring current: IMP 7/8 and ISEE 1, J. Geophys. Res., 90(A11), 10991-11008.

Roelof, E. C. (1987), Energetic neutral atom image of a storm-time ring current, Geophys. Res. Lett., 14(6), 652‑655.

Sckopke, N. (1966), A general relation between the energy of trapped particles and the disturbance field near the Earth, J. Geophys. Res., 71(13), 3125-3130.

Sergeev, V. A., E. M. Sazhina, N. A. Tsyganenko, J. A. Lundblad, and F. Søraas (1983), Pitch-angle scattering of energetic protons in the magnetotail current sheet as the dominant source of their isotropic precipitation into the nightside ionosphere, Planet. Space Sci., 31, 1147.

Sergeev, V. A., M. Malkov, and K. Mursula (1993), Testing the isotropic boundary algorithm method to evaluate the magnetic field configuration in the tail, J. Geophys. Res. 98, 7609.

Smith, P. H., and R. A. Hoffman (1973), Ring current particle distributions during the magnetic storms of December 16 - 18, 1971, J. Geophys. Res., 78(22), 4731-4737.

Spasojevic, M., M. F. Thomsen, P. J. Chi, and B. R. Sandel (2005), Afternoon subauroral proton precipitation resulting from ring current-plasmasphere interaction, in Inner Magnetosphere Interactions: New Perspectives from Imaging, Geophys. Monogr. Ser., vol. 159, edited by J. Burch, M. Schulz, and H. Spence, p. 85, AGU, Washington, D. C.

Spitzer, L. (1962), Physics of Fully Ionized Gases, Interscience, New York.

Søraas, F., K. Aarsnes, J. Å. Lundblad, and D. S. Evans, Enhanced pitch angle scattering of protons at mid-latitudes during geomagnetic storms, Phys. Chem. Earth, Part C, 24, 287,

1999.

Thomsen, M. F., J. E. Borovsky, D. J. McComas, and M. R. Collier (1998), Variability of the ring current source population, Geophys. Res. Lett., 25(18), 3481-3484.

Tinsley, B. A. (1976), Evidence that the recovery phase ring current consists of Helium ions, J. Geophys. Res., 81(34), 6193?6196, doi:10.1029/JA081i034p06193.

Tsyganenko, N. A., H. J. Singer, and J. C. Kasper (2003), Storm-time distortion of the inner magnetosphere: How severe can it get?, J. Geophys. Res., 108(A5), 1209, doi:10.1029/2002JA009808.

Tsyganenko, N. A., and M. I. Sitnov (2005), Modeling the dynamics of the inner magnetosphere during strong geomagnetic storms, J. Geophys. Res., 110 (A3), A03208, doi: 10.1029/2004JA010798.

Walt, M., and H. D. Voss (2001), Losses of ring current ions by strong pitch angle scattering, Geophys. Res. Lett., 28, 3839–3841.

Weimer, D. R. (2005), Improved ionospheric electrodynamic models and application to calculating Joule heating rates, J. Geophys. Res., 110, A05306, doi:10.1029/2004JA010884.

Wilken, B., et al. (1992), Magnetospheric ion composition spectrometer onboard the CRRES spacecraft, J. Spacecraft and Rockets, 29, 585.

Williams, D. J., and L. R. Lyons (1974), Further Aspects of the Proton Ring Current Interaction With the Plasmapause: Main and Recovery Phases, J. Geophys. Res., 79(31), 4791–4798.

Williams, D. J. (1981), Ring current composition and sources: An update, Planet. Space Sci. 29, 1195-1203

Wolf, R. A., M. Harel, R. W. Spiro, G. -H. Voigt, P. H. Reiff, and C. -K. Chen (1982), Computer simulation of inner magnetospheric dynamics for the magnetic storm of July 29, 1977, J. Geophys. Res., 87(A8), 5949-5962.

Young, S. L., R. E. Denton, B. J. Anderson, and M. K. Hudson (2002), Empirical model for μ scattering caused by field line curvature in a realistic magnetosphere, J. Geophys. Res., 107(A6), 1069, doi:10.1029/2000JA000294.

Young, S. L., R. E. Denton, B. J. Anderson, and M. K. Hudson (2008), Magnetic field line curvature induced pitch angle diffusion in the inner magnetosphere, J. Geophys. Res., 113, A03210, doi:10.1029/2006JA012133.

Table

Table 1. List of the simulation settings.

Name	Adiabatic loss cone loss	Charge exchange	FLC scattering
Run 1	Yes	Yes	Yes
Run 2	Yes	Yes	No
Run 3	Yes	No	No

Figure caption

Figure 1. From top to bottom, IMF By, IMF Bz, solar wind density (Nsw), solar wind velocity (Vsw), and Sym-H* are shown. The IMF and solar wind parameters were obtained from the 5-min resolution of the OMNI2 database, which are time-shifted to the bow shock position.

Figure 2. Calculated perpendicular plasma pressure of protons at 0840 UT on 12 August 2000. The pressure is shown in the equatorial plane, and the Sun is to the left. The outer circle corresponds to $L = 6.5$.

Figure 3. Ratio between the gyroradius of a 50 keV proton and the curvature radius of a field line and in the equatorial plane as predicted by the TS04 magnetic field model for the condition corresponding to 0840 UT on 12 August 2000.

Figure 4. Calculated pitch angle distribution of 50 keV protons as a function of equatorial pitch angle at midnight at $L = 4$ (left) and $L = 5$ (right) for Run 1 (thick line) and Run 2 (thin line).

Figure 5. Energy flux of precipitating protons at the ionosphere altitude at 0840 UT on 12 August 2000. The energy flux was obtained from auroral images acquired by the IMAGE

satellite (left), and simulations for Run 1 (left) and Run 2 (middle).

Figure 6. Observed Dst* index (top) and the power of the precipitating protons (bottom). The solid, dotted, and dashed lines indicate the observed values and those simulated for Run 1 and Run 2, respectively.

Figure 7. Observed Sym-H* (black) and simulated ones for Run 1 (red), Run 2 (blue), and Run 3 (green).

Figure 8. Composite images of energetic hydrogen (reddish color) and precipitating protons (bluish color) from the vantage point of the IMAGE satellite at (0.4, 0.7, 5.7) R_E in the SM coordinates at 0840 UT on 12 August 2000. Panel (a) shows the images of energetic hydrogen observed by IMAGE/HENA (39–50 keV) and precipitating protons observed by IMAGE/FUV, panel (b) shows the simulated ones for Run 1, and panel (c) shows the simulated ones for Run 2. Unit for energetic hydrogen is 1/cm^2 s str keV, and unit for precipitating protons is 10^{12} eV/cm^2 s. Dipole field lines for L = 3 and 6.6 are drawn at 0000, 0600, 1200, and 1800 MLT. The outer circle corresponds to L = 6.6 and the inner circle represents the surface of the Earth.

Figure 9. Integrated energetic neutral hydrogen flux with energy (a) 10–39 keV and (b) 39–119 keV. A solid line shows the one observed by IMAGE/HENA. Dotted and dashed lines show the simulated one in Run 1 and Run 2, respectively.

Figures

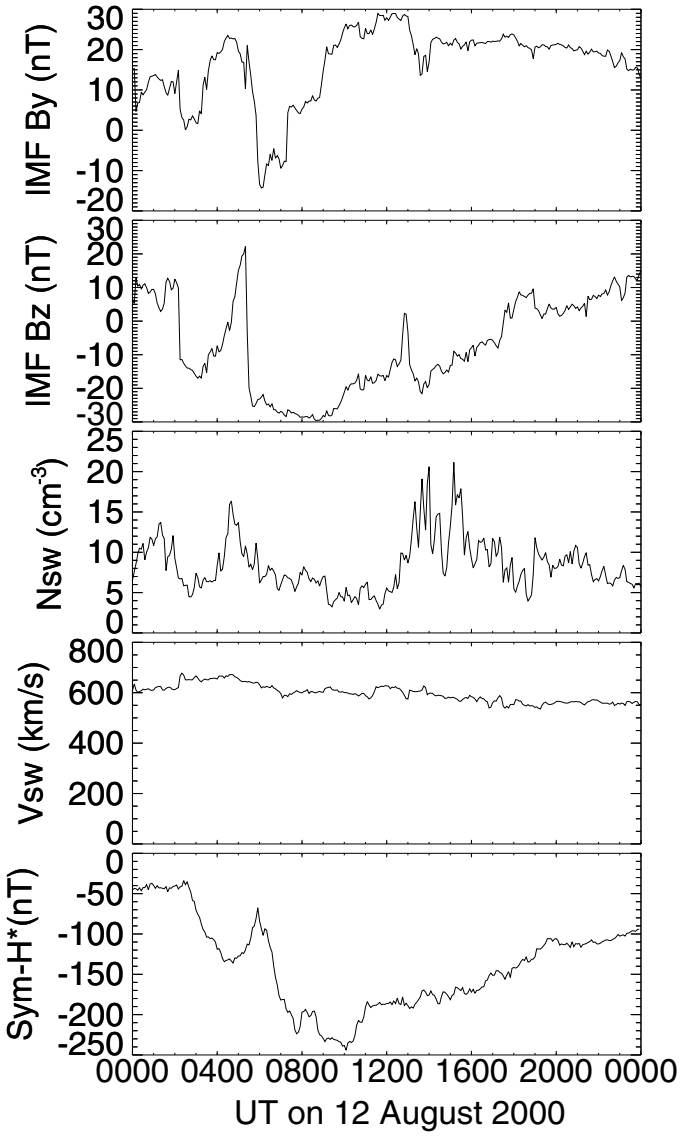

Figure 1. From top to bottom, IMF By, IMF Bz, solar wind density (Nsw), solar wind velocity (Vsw), and Sym-H* are shown. The IMF and solar wind parameters were obtained from the 5-min resolution of the OMNI2 database, which are time-shifted to the bow shock position.

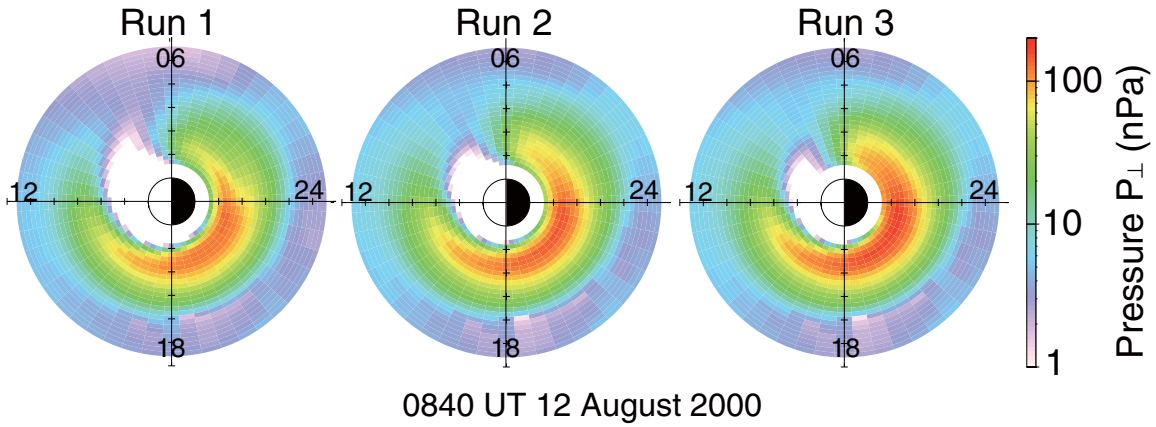

Figure 2. Calculated perpendicular plasma pressure of protons at 0840 UT on 12 August 2000. The pressure is shown in the equatorial plane, and the Sun is to the left. The outer circle corresponds to L = 6.5.

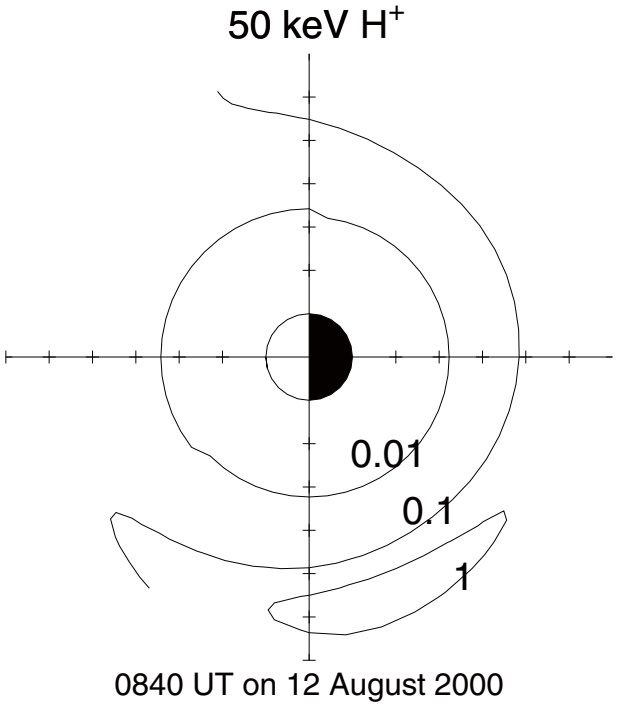

Figure 3. Ratio between the gyroradius of a 50 keV proton and the curvature radius of a field line and in the equatorial plane as predicted by the TS04 magnetic field model for the condition corresponding to 0840 UT on 12 August 2000.

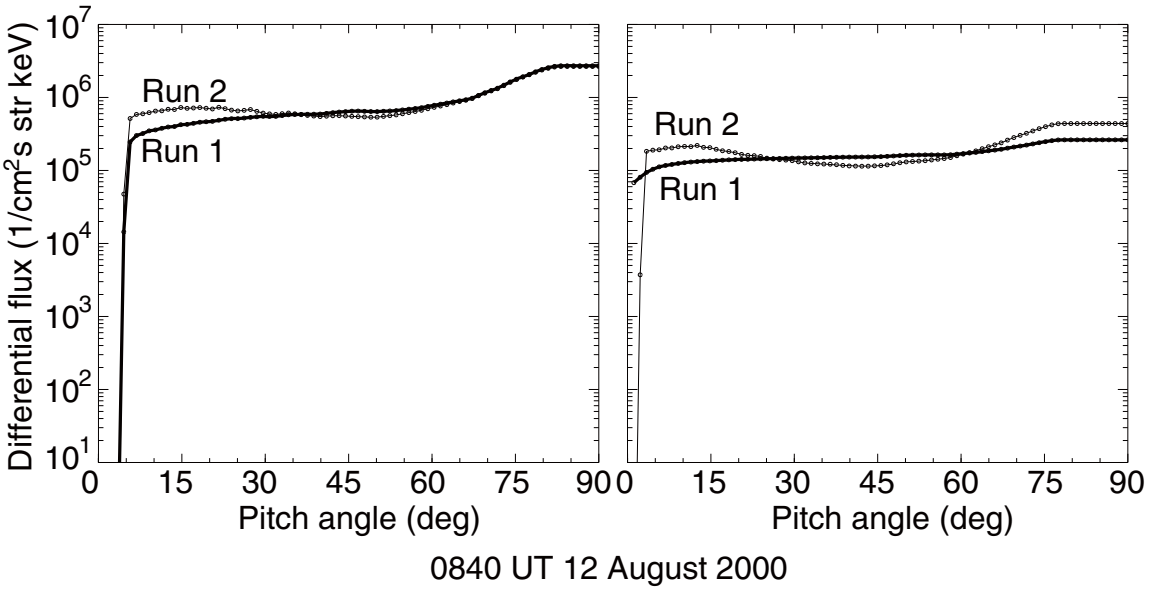

Figure 4. Calculated pitch angle distribution of 50 keV protons as a function of equatorial pitch angle at midnight at L = 4 (left) and L = 5 (right) for Run 1 (thick line) and Run 2 (thin line).

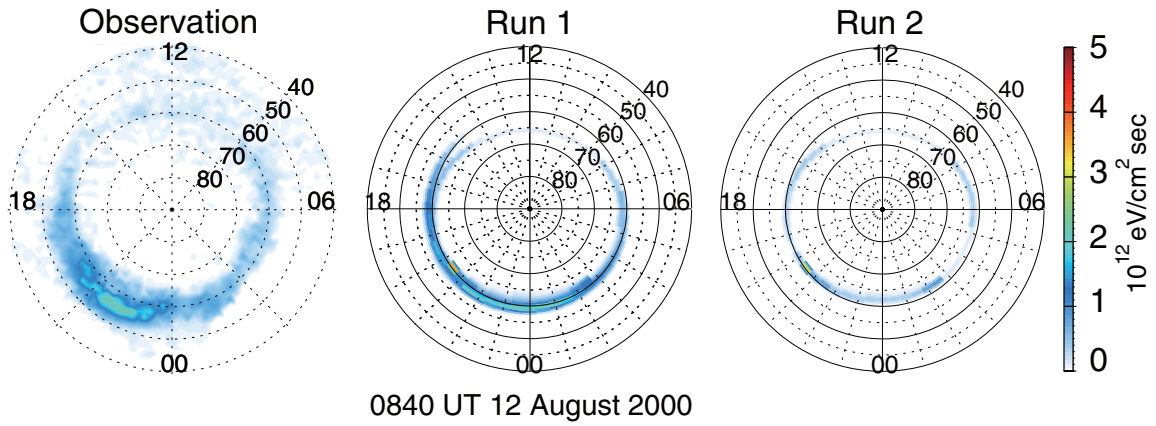

Figure 5. Energy flux of precipitating protons at the ionosphere altitude at 0840 UT on 12 August 2000. The energy flux was obtained from auroral images acquired by the IMAGE satellite (left), and simulations for Run 1 (left) and Run 2 (middle).

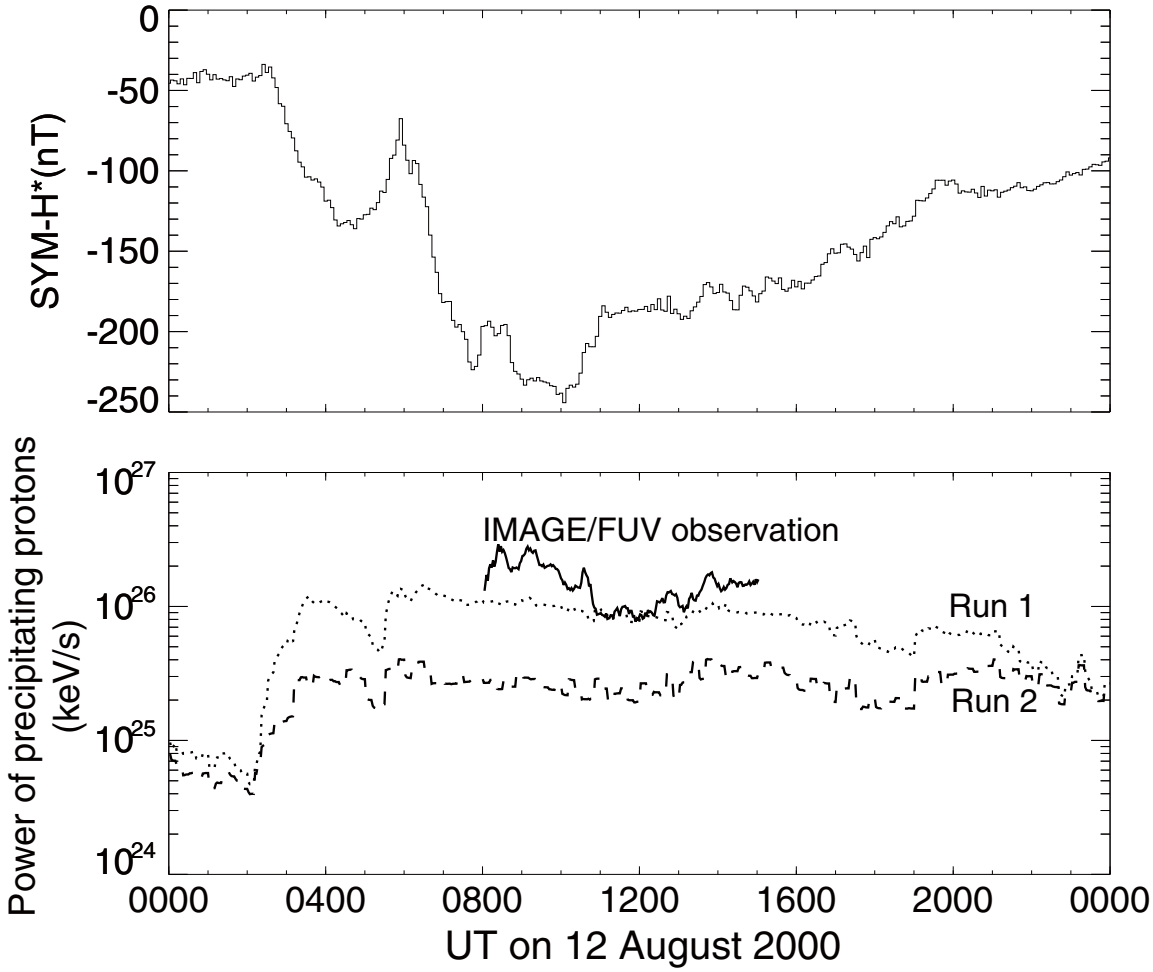

24 **Figure 6.** Observed Dst* index (top) and the power of the precipitating protons (bottom).

25 The solid, dotted, and dashed lines indicate the observed values and those simulated for

26 Run 1 and Run 2, respectively.

27

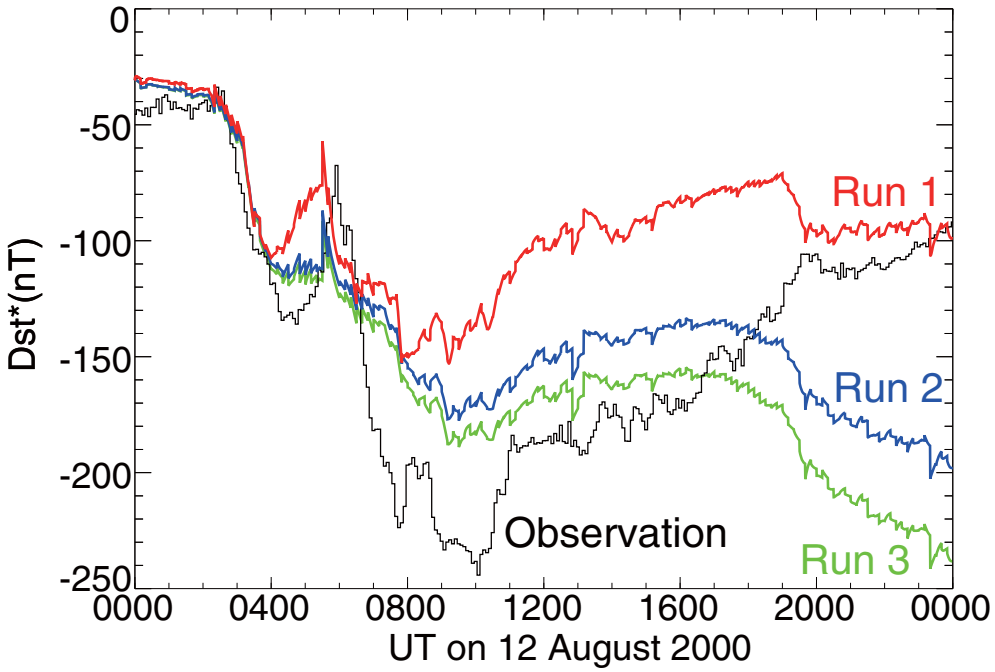

28 **Figure 7.** Observed Sym-H* (black) and simulated ones for Run 1 (red), Run 2 (blue),

29 and Run 3 (green).

30

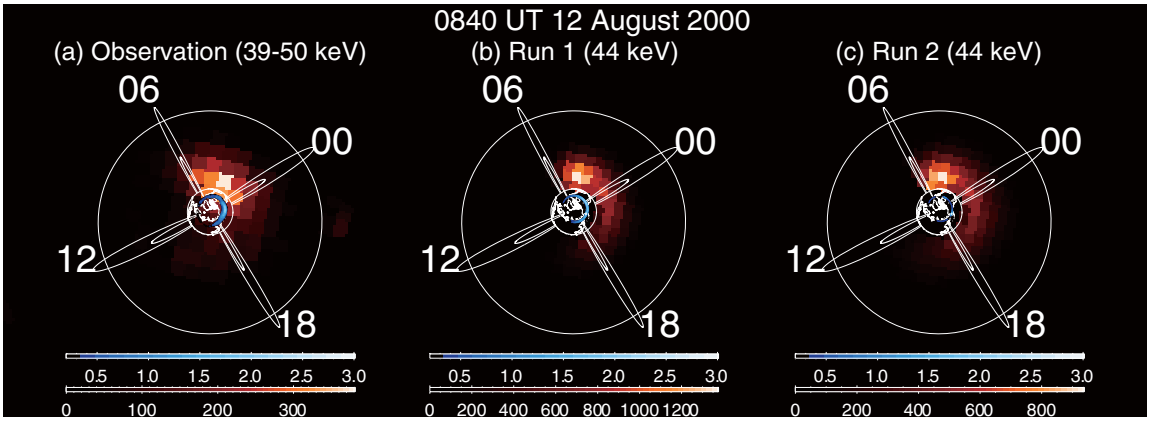

Figure 8. Composite images of energetic hydrogen (reddish color) and precipitating protons (bluish color) from the vantage point of the IMAGE satellite at (0.4, 0.7, 5.7) R_E in the SM coordinates at 0840 UT on 12 August 2000. Panel (a) shows the images of energetic hydrogen observed by IMAGE/HENA (39–50 keV) and precipitating protons observed by IMAGE/FUV, panel (b) shows the simulated ones for Run 1, and panel (c) shows the simulated ones for Run 2. Unit for energetic hydrogen is 1/cm^2 s str keV, and unit for precipitating protons is 10^{12} eV/cm^2 s. Dipole field lines for L = 3 and 6.6 are drawn at 0000, 0600, 1200, and 1800 MLT. The outer circle corresponds to L = 6.6 and the inner circle represents the surface of the Earth.

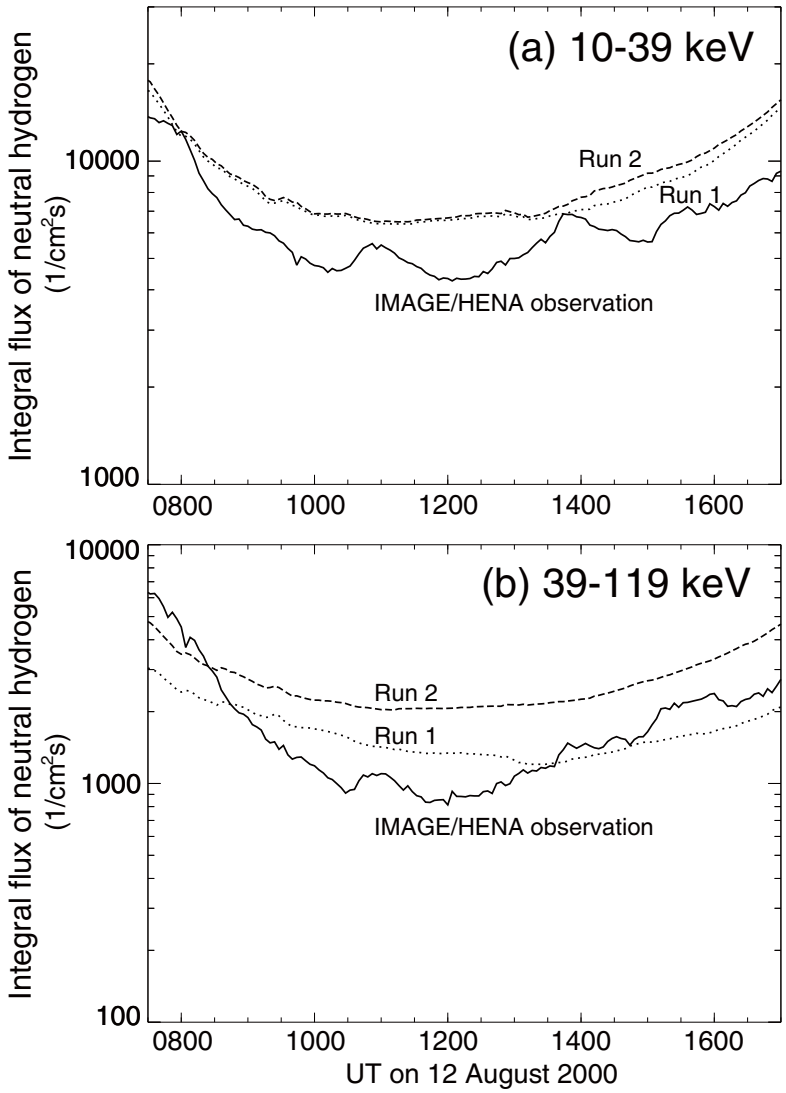

41 **Figure 9.** Integrated energetic neutral hydrogen flux with energy (a) 10–39 keV and (b)
42 39–119 keV. A solid line shows the one observed by IMAGE/HENA. Dotted and
43 dashed lines show the simulated one in Run 1 and Run 2, respectively.